

# ACCRETION ONTO THE SUPERMASSIVE BLACK HOLE IN THE HIGH-REDSHIFT RADIO-LOUD AGN 0957+561

RODRIGO GIL-MERINO, LUIS J. GOICOECHEA, VYACHESLAV N. SHALYAPIN<sup>1</sup> AND VITTORIO F. BRAGA  
Departamento de Física Moderna, Universidad de Cantabria, Avda. de Los Castros s/n, 39005 Santander, Spain

*Submitted to ApJ*

## ABSTRACT

We present the results of our X-ray, UV and optical monitoring campaign of the first gravitationally lensed AGN from late 2009 to mid 2010. The trailing (B) image of the AGN 0957+561 shows the intrinsic continuum variations that were predicted in advance based on observations of the leading (A) image in the *gr* optical bands. This multiwavelength variability of the B image allows us to carry out a reverberation mapping analysis in the radio-loud AGN 0957+561 at redshift  $z = 1.41$ . We find that the *U*-band and *r*-band light curves are highly correlated with the *g*-band record, leading and trailing it by  $3 \pm 1$  days (*U* band) and  $4 \pm 1$  days (*r* band). These  $1\sigma$  measurements are consistent with a scenario in which flares originated in the immediate vicinity of the supermassive black hole are thermally reprocessed in a standard accretion disk at  $\sim 10$ – $20$  Schwarzschild radii from the central dark object. We also report that the light curve for the X-ray emission with power-law spectrum is delayed with respect to those in the *Ugr* bands by  $\sim 32$  days. Hence, the central driving source can not be a standard corona emitting the observed power-law X-rays. This result is also supported by X-ray reprocessing simulations and the absence of X-ray reflection features in the spectrum of 0957+561. We plausibly interpret the lack of reflection and the 32-day delay as evidence for a power-law X-ray source in the base of the jet at a typical height of  $\sim 200$  Schwarzschild radii. A central EUV source would drive the variability of 0957+561.

*Subject headings:* accretion — black hole physics — gravitational lensing: strong — quasars: individual: 0957+561

## 1. INTRODUCTION

In the accretion paradigm for AGNs, viscous dissipation in a standard (geometrically thin and optically thick) accretion disk is responsible for UV-optical continuum emission (Shakura & Sunyaev 1973). Moreover, in this paradigm, the X-ray emission with power-law spectrum is produced in a standard corona on the rotation axis just above the black hole. The coronal X-ray photons are then partially reflected and thermally reprocessed into UV-optical continuum radiation in the disk (Collin-Souffrin 1991; George & Fabian 1991). Thus, coronal power-law X-ray fluctuations with timescales  $\leq 100$  days in the source rest-frame are expected to drive UV-optical short-timescale events (e.g., see the formalism of Kazanas & Nayakshin 2001). However, the precise origin and geometrical distribution of the X-ray, UV and optical energy production are still largely unknown.

Direct spatial resolution of the accretion flow in AGNs is not currently possible (e.g., Krolik 1999), so we must use indirect techniques to resolve the emitting regions. Fortunately, reverberation (or echo) mapping is a promising time-domain technique to probe the accretion physics for AGNs. This is based on the analysis of time-delayed responses of different emitting regions to original fluctuations in a driving source (Blandford & McKee 1982; Netzer & Peterson 1997). Concurrent X-ray-UV-optical continuum monitoring campaigns of low-redshift AGNs led to puzzling findings. In gen-

eral, the fastest (days) X-ray and UV-optical variations matched up poorly (e.g., Maoz et al. 2000; Gaskell 2006; Breedt et al. 2009). On the other hand, the slowest (tens of days) multiwavelength variability yielded ambiguous results, sometimes supporting the accretion paradigm (e.g., Breedt et al. 2009), often suggesting otherwise (e.g., Maoz et al. 2000; Gaskell 2006; Arévalo et al. 2009). The situation is even less clear for AGNs at redshift  $z \geq 1$ , since there are no X-ray-UV-optical reverberation studies of these objects.

The amount of radio emission and the presence of relativistic jets divide active galactic nuclei in radio-quiet AGNs (RQAGNs) and radio-loud AGNs (RLAGNs). RLAGNs represent only the 10% of all known AGNs. They display relativistic jets, likely launched from regions on the rotation axes of their central supermassive black hole (e.g., Urry 2003). Thus, while RLAGNs having one jet closely aligned with the line of sight (the so-called blazars or jet-dominated RLAGNs) are used to probe the jet physics (e.g., Urry 1998), RLAGNs with a relatively large inclination angle (accretion-dominated RLAGNs) are key tools to unveil the accretion onto black holes in AGNs displaying jets (Landt et al. 2008).

The RLAGN 0957+561 at  $z = 1.41$  suffers a strong gravitational lens effect (Walsh et al. 1979). The gravitational field of a foreground galaxy cluster produces two images, A and B, of the same background AGN. A and B arrive at the observer at different times, with intrinsic flux variations in B lagging those in A by about 14 months (e.g., Kundic et al. 1997). This is an exceptional fact that offers two fundamental advantages with respect to non-lensed AGNs: first, if we detect large flux variations in A a multiwavelength campaign can be planned to fol-

Electronic address: r.gilmerino@gmail.com, luis.goicoechea@unican.es

<sup>1</sup> permanent address: Institute for Radiophysics and Electronics, National Academy of Sciences of Ukraine, 12 Proskura St., 61085 Kharkov, Ukraine

low the variability in B one year later; second, if flux variations in A are indeed intrinsic to the AGN, similar fluctuations must also appear in B and we know that these are exclusively associated to the AGN physics. Moreover, radio observations of the jet in 0957+561 suggested a small beaming factor (Campbell et al. 1994), and hence, an accretion-dominated X-ray–UV–optical emission towards the observer (Landt et al. 2008).

We are monitoring 0957+561 in the optical range since the year 2005 with the Liverpool Robotic Telescope (LRT), as part of a large gravitational lenses project (Shalyapin et al. 2008). Observations in late 2008 and the first semester of 2009 showed significant variations in image A, whose *g*-band flux increased  $\sim 30\%$  just after a deep minimum. Assuming an intrinsic origin for the optical fluctuations in A, we were then able to predict a strong variability during the first semester of 2010 in image B (Goicoechea & Shalyapin 2009). To take this opportunity, we organized an ambitious multiwavelength follow-up campaign. This included observations with the space-based telescopes Chandra and Swift/UVOT for X-rays and UV, respectively, and with the ground-based LRT in the *g* and *r* optical bands<sup>2</sup>. In Section 2 we present these observations and the corresponding light curves. Preliminary records of B indicated the intrinsic origin of the observed variations (see Fig. 2 of Goicoechea et al. 2011), so the reverberation mapping analysis in Section 3 unveils the nature of the accretion flow and its jet connection in a distant RLAGN for the first time. In Section 4 we present our main conclusions.

## 2. OBSERVATIONS AND LIGHT CURVES

At optical wavelengths we used the LRT. This is a ground-based fully-robotic 2m telescope (Steele et al. 2004) at La Palma, Canary Islands, which is one of the world's best astronomical sites (Muñoz-Tuñón et al. 1997). All LRT optical frames were obtained between 2009 December 26 and 2010 June 25 with the RATCam CCD camera in the *gr* Sloan passbands (see Table 1). In order to get a typical signal-to-noise ratio of  $\sim 100$  for both AGN images for each observing night, we set the exposure times to 120 s per night in both bands. The pre-processing steps included in the LRT pipeline are: bias subtraction, overscan trimming and flatfielding. In addition, we interpolate over bad pixels using the bad pixel mask and clean some cosmic rays. The pre-processed frames are then analyzed using our photometric pipelines (Shalyapin et al. 2008): the crowded-field photometry pipeline produces instrumental point spread function (PSF) magnitudes of the AGN images, while an additional pipeline transforms instrumental magnitudes into Sloan Digital Sky Survey (SDSS) magnitudes. Ultimately, we turn magnitudes into fluxes (in mJy) using SDSS conversion equations<sup>3</sup>.

We obtain 55 *g*-SDSS fluxes for each image with accuracies of 1.2% (A) and 1.3% (B), as well as 58 *r*-SDSS fluxes for each image with accuracies of 1.0% (A) and 1.1% (B). This variability database is available in tabu-

lar format at the GLENDAMA Web site<sup>4</sup>. The optical light curves of 0957+561B are depicted in the top panel of Fig. 1 (squares and circles). As a result of the cosmic expansion, observed wavelengths are longer than emission wavelengths at the AGN. Thus, our optical observations correspond to far and middle UV continuum sources at  $z = 1.41$ .

We also used the UV/Optical Telescope (UVOT) on board the satellite Swift (Roming et al. 2005) to observe 0957+561 in the near UV. A total of 35 *U*-band CCD frames were obtained between 2010 January 12 and 2010 June 1 (see Table 1), and we show one of them in Fig. 2. The exposure time varied in the range of 155–1092 s, with a median value of  $\sim 500$  s. We reduce the observations from standard HEASoft packages<sup>5</sup>. The UVOTSOURCE task is used for performing aperture photometry on point-like objects. This task incorporates a coincidence-loss correction, which is important even for relatively faint objects (Li et al. 2006). Taking into account the size of the PSF (full-width at half maximum of about  $2''.5$ ) and the  $\sim 6''$  separation of the AGN images, we choose an aperture radius of  $3''$ . However, the UVOT calibration is based on counts measured within a  $5''$  aperture, so an aperture correction is required (Poole et al. 2008). This correction depends on the PSF of the object of interest which in turn depends on the brightness, position and time (Li et al. 2006; Poole et al. 2008). We estimate the aperture correction for each exposure, using the PSF of the nearest star to the lensed AGN. This H star has a brightness similar to that of the AGN images, A and B. We also check the stability of three reference bright stars close to H (see A, B, H and stars XFG in Fig. 2). The *U*-UVOT fluxes (in mJy) of 0957+561 are available at the GLENDAMA Web site<sup>3</sup>, and the light curve of B is shown in the top panel of Fig. 1 (triangles).

Observations in X-rays were obtained via Director's Discretionary Time with the space-based Chandra Observatory (Weisskopf et al. 2002). They were carried out every other week from January 17 to June 23 in 2010 with the ACIS-S3 detector, resulting in 12 datasets evenly spaced with an exposure time of  $\sim 3$  ks each (see Table 1). X-ray spectra are then extracted for images A and B and the corresponding background fields using standard routines from the CIAO 4.3 software<sup>6</sup>. The regions for AGN spectra extraction are  $\sim 2''.5$  in radius centered at the peak of the emission; the backgrounds are  $\sim 3''$  in radius, located close to the source extraction regions. We test different positions for the background regions, finding no significant differences. The regions are always located at the same coordinates from dataset to dataset. At this stage, for extraction purposes, we consider the energy range from 0.1 to 11 keV in the observer rest-frame. We also check for possible pile-up<sup>5</sup> but we find none, surely due to the short exposure time of individual snapshots.

To investigate the fiducial model underlying the AGN X-ray emission, for each AGN image, we combine all the individual spectra to obtain a single high signal-to-noise one. In doing this, we identify the features that are com-

<sup>2</sup> We also observed 0957+561B with the LRT in the *i* and *z* bands. However, in this paper we only discuss the best data from each telescope. The photometric accuracy and time coverage in the *iz* Sloan passbands are worse than those in the *gr* Sloan passbands.

<sup>3</sup> <http://www.sdss.org/dr7/algorithms/fluxcal.html>.

<sup>4</sup> [http://grupos.unican.es/glendama/LQLMII\\_DR.htm](http://grupos.unican.es/glendama/LQLMII_DR.htm).

<sup>5</sup> <http://heasarc.nasa.gov/heasoft/>.

<sup>6</sup> <http://cxc.harvard.edu/ciao/>.

mon to both AGN images in all frames and thus the emission model components that explain the X-ray sources; then we use that model to fit all the individual frames, studying in this way how the different components of the model vary with time. In the energy range 0.1–10 keV in the observer’s frame, an absorbed power-law model (Chartas et al. 2002) produces uncomfortable fits to the global spectra of A and B (dashed lines in Fig. 3). To improve the fits, we introduce a power-law plus blackbody radiation at the redshift of the distant AGN, both affected by Galactic neutral absorption ( $N_{\text{H}} = 8.2 \times 10^{19} \text{ cm}^{-2}$ ; Dickey & Lockman 1990). We then obtain  $1\sigma$  parameter values:  $\Gamma = 1.775 \pm 0.035$  and  $kT = 0.07 \pm 0.02 \text{ keV}$  (best fit:  $\chi^2/\text{dof} = 1.03$ , dof = degrees of freedom) for A, and  $\Gamma = 1.790 \pm 0.035$  and  $kT = 0.085 \pm 0.030 \text{ keV}$  (best fit:  $\chi^2/\text{dof} = 0.93$ ) for B, where  $\Gamma$  is the photon index of the power-law and  $kT$  is the blackbody temperature. There is no evidence for absorption exceeding the Galactic value, and the blackbody radiation is necessary to account for the soft excess detected below 0.5 keV. Both fits agree with each other, so we take the average values  $\Gamma = 1.78$  and  $kT = 0.08 \text{ keV}$  as the best model parameters for representing the AGN X-ray emission (solid lines in Fig. 3). We also check for other two-component models consisting of a power-law plus additional emission. For example, a two power-law model leads to worse fits for reasonable photon indices.

The X-ray variability of the B image is obtained by fitting its individual spectra to our best X-ray emission model, and leaving as free parameters the normalization of the two model components, i.e., power-law and blackbody. We compute then the flux contribution of the power-law and blackbody emissions separately. We use the energy ranges 2–10 keV and  $\leq 1 \text{ keV}$  for the power-law and blackbody emissions, respectively, both at the source rest-frame. Several tests with different two-component models give rise to light curves similar in shape to those from our best model. The power-law and blackbody fluxes of 0957+561 are available at the Web site of the GLENDAMA project<sup>3</sup>. In the bottom panel of Fig. 1, we display two X-ray light curves of 0957+561B. While circles represent the observed power-law fluxes (2–10 keV emission), the dashed line describes the unabsorbed power-law fluxes in the same energy range. In Fig. 4 we also see noisy blackbody fluxes of 0957+561B. These fluxes ( $\leq 1 \text{ keV}$  emission) are substantially smaller than the power-law ones, and have large uncertainties of 30–70%.

### 3. CONTINUUM REVERBERATION MAPPING IN 0957+561

#### 3.1. Cross-correlation analysis

The cross-correlation function permits a fair estimation of the time delay or time lag between two signals. For determining the delay between two discrete data trains, Edelson & Krolik (1988) introduced the discrete cross-correlation function (*DCF*), which we use in our analysis. The *DCF* is characterized by a bin semisize  $\alpha$ , and one must check how different  $\alpha$  values affect its form. Consecutive independent bins are separated by two times  $\alpha$ . However, there is an ambiguity in the choice of central lags of bins, so these lags can be shifted in an amount  $< 2\alpha$  to the left or right of any initial values. The same is true for the discrete autocorrelation function (*DAF*). Because of such ambiguity, both the *DCF* and *DAF* are

evaluated in almost continuous sets of bins. Although nearby bins are not independent, this procedure exclusively relies on measured fluxes and correlations. Other methods such as interpolating (or fitting) the light curves or the *DCF/DAF* yield unmeasured fluxes or correlations.

The time delay is given by the centroid of the *DCF* peak. Besides the delay, the two signals may differ in shape. If they are related through simple effective parameters: a flux offset and a multiplicative factor, the broad and irregular delay-peak should be closely traced by the symmetrical peak around zero lag of the *DAF*. Hence, the time-shifted peak of the *DAF* can be matched to the *DCF* peak to estimate the delay in a self-consistent way. The time delay corresponds to the minimum of the so-called  $\delta^2$  function, i.e. the minimum of the square difference between the *DCF* and the time-shifted *DAF* (e.g., Serra-Ricart et al. 1999). We follow a standard Monte Carlo approach to generate synthetic light curves and determine time delay errors. We make 1000 repetitions of the experiment by adding random quantities to the original fluxes in the light curves. The random quantities are realisations of normal distributions around zero, with standard deviations equal to the errors of the fluxes. For each pair of curves in Fig. 1: *ab*, where  $a, b = g, r, U, X$ , a negative delay  $\Delta\tau_{ab} = \tau_b - \tau_a < 0$  means that *b* is leading, while a positive delay  $\Delta\tau_{ab} > 0$  means the opposite (*b* trailing).

We initially focus on the *gU* and *gr* comparisons, i.e., the *g*-band light curve is compared to the other two UV-optical brightness records. Firstly, in order to measure the *gU* time delay, we consider  $\alpha = 5$ –25 days. We find that both the *DAF* and *DCF* peaks are smoother for longer bins, but the relationship between the two remains basically unchanged and their maxima always exceed 0.8. We also find that all  $\delta^2$  functions indicate a negative delay (*U* leading). These  $\delta^2$  functions are particularly narrow for  $\alpha = 10$ –12 days (see Fig. 5), so we compute the delay and its errors using  $\alpha = 10$  days. Secondly, we compare the records in the *g* and *r* bands. The *DAF* and *DCF* peaks for  $\alpha = 5$ –25 days again show maxima exceeding 0.8. However, this time the  $\delta^2$  functions are consistent with a positive delay (*r* trailing). The bin semisizes  $\alpha = 18$ –20 days produce narrow  $\delta^2$  functions (see Fig. 6), and we estimate the *gr* delay using  $\alpha = 20$  days. We note that a relatively long bin is required to tighten the  $\delta^2$  curve. This could be due to the presence of a few small gaps ( $\sim 10$ –20 days) in both light curves.

At the redshift of 0957+561, the C IV ( $\lambda 1549$ ), C III] ( $\lambda 1909$ ) and Mg II ( $\lambda 2798$ ) emission lines lie in spectral regions covered by the *U*, *g* and *r* filters, respectively (Walsh et al. 1979). Therefore, one might think that the observed delays between the UV-optical light curves are associated with variations of lines rather than changes in the continuum. To check the contribution of the continuum and emission lines to our fluxes, we reduce and analyze new Nordic Optical Telescope (NOT) spectra of 0957+561B. These were taken on 2010 March 28, in the middle of our monitoring campaign (see Table 1) and covering the *gr* filters. From the NOT data, we infer continuum-to-total ratios of  $\sim 0.97$  in the *g* and *r* bands. Thus, the emission line contamination is typically about 3%, representing a very small fraction of the optical fluxes.

We also study the time delays between the power-law X-ray curve and the three UV-optical records. The pair of curves  $XU$  leads to  $DCF$  peaks with maxima of  $\sim 0.8$  for  $\alpha = 10$ –25 days. However, the  $\delta^2$  function is relatively broad for these bins.  $DCF$  maxima are only reduced to  $\sim 0.7$  for longer bins with  $\alpha \sim 30$  days, but the corresponding  $\delta^2$  curves are clearly narrower. Thus, we take  $\alpha = 30$  days to measure the  $XU$  delay (see top panels of Fig. 7). There is an evident time shift of  $\sim 30$  days between the  $DAF$  and  $DCF$  peaks, which is detected for any value of  $\alpha$ . This time shift produces a minimum in  $\delta^2$  at about  $-30$  days, suggesting a negative delay ( $U$  leading) of about one month. The other two comparisons yield similar results using  $\alpha = 45$  days (see middle and bottom panels of Fig. 7). For the two pairs of curves  $Xg$  and  $Xr$ ,  $DCF$  maxima have values of  $\sim 0.5$ – $0.6$  over a wide range of  $\alpha$ , i.e.,  $\alpha = 10$ – $50$  days, and  $\delta^2$  functions are broader than those for the  $XU$  pair.

In addition to the X-ray/UV-optical delays, we assess the significance of the relatively low cross-correlation peaks in Fig. 7. For the  $XU$  comparison, the maximum correlation is 0.7. This corresponds to two time series consisting of  $N_X = 12$  and  $N_U = 35$  points. Assuming a number of pairs of data  $N = (N_X + N_U)/2 \sim 23$ , the correlation is significant at about the 99.98% confidence level. In other words, uncorrelated data are very unlikely ( $\sim 0.02\%$ ) to produce a correlation  $\geq 0.7$  (e.g., Taylor 1997). Moreover, completely uncorrelated time series would generate a  $DCF$  noise of  $\sim 0.08$ – $0.09$  (Edelson & Krolik 1988), which is well below the filled circles in the top left panel of Fig. 7. For the  $Xg$  and  $Xr$  comparisons, the maximum correlation slightly exceeds 0.5. If we consider  $N \sim 34$  ( $N_g = 55$  and  $N_r = 58$ ), then the correlation is significant at about the 99.7% confidence level. The  $DCF$  noise is  $\sim 0.06$ – $0.07$ , and the signal-to-noise ratio in both  $DCF$  peaks reaches values in the interval 3–10.

How do 0957+561 cross-correlation results fit into the accretion paradigm for AGNs and the associated rapid variability? We produce 1000 synthetic light curves for each observed record in Fig. 1. In each synthetic curve, the observed fluxes are modified by random Gaussian deviations that are consistent with the measured uncertainties (see above). Thus, we obtain 1000 delay values for each pair  $gU$ ,  $gr$ ,  $XU$ ,  $Xg$  and  $Xr$ . The corresponding delay histograms are drawn in Fig. 8. For the pairs  $gU$  (prominent peak around  $-3$  days) and  $gr$  (prominent peak around 4 days), their delay distributions are narrower than those involving the X-ray record. From these narrow distributions, we infer  $1\sigma$  uncertainties (68% confidence intervals) of only  $\pm 1$  day. Thus,  $\Delta\tau_{gU} = -3 \pm 1$  days and  $\Delta\tau_{gr} = 4 \pm 1$  days (see Table 2), indicating that  $U$  is leading and  $r$  is trailing. These band-to-band lags are consistent with delays  $\tau(\lambda) \propto \lambda^{4/3}$  between a central driving source and standard disk rings emitting at different wavelengths  $\lambda$  (e.g., Collier et al. 1999). One can easily obtain the delays  $\tau(1438 \text{ \AA}) = 6$  days,  $\tau(1944 \text{ \AA}) = 9$  days and  $\tau(2558 \text{ \AA}) = 13$  days, which put the far and middle UV continuum sources at radii  $R = c\tau/(1+z)$  of a few thousandths of a pc ( $c$  is the speed of light). Our  $gU$  and  $gr$  cross-correlation studies confirm some previous evidences in favour of thermal reprocessing in a standard accretion disk (Collier 2001;

Shalyapin et al. 2008).

For the pair  $gU$ , its delay distribution in Fig. 8 indicates that  $U$  is leading (negative delay) at about the  $3\sigma$  level. Moreover, the  $gr$  delay for 0957+561B is now robust because there are two independent estimates agreeing with each other:  $4.0^{+1.0}_{-1.7}$  days (Apache Point Observatory data and interpolated cross-correlation function; Collier 2001), and  $4 \pm 1$  days (LRT data and  $DCF$ ; this paper). Apart from the  $DCF$  as implemented by us, we use a  $\chi^2$  method (e.g., Kundic et al. 1997; Shalyapin et al. 2008) to compare the light curves in the  $g$  and  $r$  bands. The key idea was to check the  $DCF$  time lag, and to obtain effective parameters (flux offset and multiplicative factor; see above) for the  $g$ -band curve. The  $\chi^2$  method produces a delay of 4 days, which is identical to that from the  $DCF$ . We also infer a flux offset of 0.21 mJy and a demagnification factor of 0.72. In the top panel of Fig. 9 we display the corrected version of  $g$  (squares) and the original version of  $r$  (circles). There is very good agreement between both trends.

The broader distributions in Fig. 8 correspond to the  $XU$  (solid line),  $Xg$  (dashed-dotted line) and  $Xr$  (dotted line) pairs. Through these distributions of delays, we determine the shortest intervals containing 68% of simulated values. The three  $1\sigma$  measurements are  $\Delta\tau_{XU} = -31 \pm 3$  days,  $\Delta\tau_{Xg} = -35.5 \pm 4.5$  days and  $\Delta\tau_{Xr} = -31 \pm 5$  days (see Table 2). Thus, the power-law X-ray curve is delayed with respect to the UV-optical curves by  $\sim 32$  days. In the standard accretion scenario for AGNs, the observed power-law X-rays are emitted from a standard corona near the central black hole. It is also believed that coronal flares are thermally reprocessed into UV variations in the inner disk to produce the observed UV-optical variability (see Section 1). In this scenario we should see the X-ray fluctuations preceding the UV-optical ones, which we do not see. Therefore, the central driving source is not a standard corona. In the next subsections, we present additional evidence supporting this result, interpret the 32-day delay and discuss the origin of the central emission. The  $\chi^2$  method for the  $XU$  pair leads to a time lag that equal the delay estimation via the  $DCF$ , i.e.,  $-31$  days. Using 0.09 mJy and 0.82 as flux offset and demagnification factor, respectively, we obtain a corrected version of  $X$  (circles and line in the bottom panel of Fig. 9) that is roughly consistent with the original version of  $U$  (triangles in the bottom panel of Fig. 9). However, some very rapid fluctuations in the curve  $X$  do not have counterparts in the curve  $U$ .

### 3.2. Simulations of X-ray reprocessing

We consider a Newtonian geometrically-thin and optically-thick accretion disk, which is illuminated by a standard corona, i.e., an isotropic power-law X-ray source just above the central black hole. This lampost model produces a radial disk temperature profile that is a non-linear combination of temperature resulting from viscous heating,  $T_{vis}$ , and that resulting from irradiation heating,  $T_{irr}$  (e.g., Collier et al. 1999; Kazanas & Nayakshin 2001).  $T_{vis}$  is governed by the black hole mass  $M$  and the mass accretion rate  $\dot{M}$ , whereas  $T_{irr}$  depends on the height  $H_X$  and luminosity  $L_X$  of the corona, as well as the disk reflectivity  $A$ . Here,  $1 - A$  represents the fraction of the X-ray radiation that is absorbed by the disk and reprocessed into UV-optical radiation.

In this subsection, we focus on the lamppost model predictions for 0957+561. The  $z = 1.41$  RLAGN 0957+561 harbours a supermassive black hole with a mass  $M = 2.5 \times 10^9 M_\odot$  (average of estimates through two emission lines; Peng et al. 2006). The corresponding Schwarzschild radius is given by  $R_S = 2GM/c^2 = 2.5 \times 10^{-4}$  pc, where  $G$  is the gravitational constant. For this high value of  $M$ , the expected  $\dot{M}$  is  $1\text{--}10 M_\odot \text{ yr}^{-1}$  (McLure & Dunlop 2004). Moreover,  $H_X < 10R_S$ , and the coronal luminosity in the 0.01–100 keV interval can be retrieved from a suitable extrapolation of the 2–10 keV unabsorbed fluxes in the bottom panel of Fig. 1 and the flux–luminosity relationship in the presence of lens magnification. The gravitational lens magnification of the B image is  $\mu_{lens} = 1.33$  (Pelt et al. 1998), and we use a concordance cosmology (Spergel et al. 2007). The cold, neutral matter has a small reflectivity  $A = 0.2$  (e.g., Magdziarz & Zdziarski 1995). In Fig. 10 we show temperature (top panel) and emission (bottom panel) profiles of the irradiated disk for typical values of the mass accretion rate ( $\dot{M} = 5 M_\odot \text{ yr}^{-1}$ ), as well as the height ( $H_X = 3R_S$ ) and luminosity (typical  $L_X$  is based on the average unabsorbed flux; see above) of the corona. We find that the disk temperature is mainly due to viscous heating, so irradiation plays a secondary role. In addition, more than 99% of the blackbody emission at  $\lambda = 1438 \text{ \AA}$  ( $U$  band) and  $\lambda = 1944 \text{ \AA}$  ( $g$  band) occurs within  $50 R_S$  of the black hole. About 97% of the radiation at  $\lambda = 2558 \text{ \AA}$  ( $r$  band) is also produced at  $R \leq 50R_S$ .

We note that the total luminosity of the corona over 0.01–100 keV includes photons in the extreme UV (EUV) and X-ray regions. However, we label this coronal emission as X-ray radiation for simplicity. In spite of the secondary role of the X-ray irradiation in the total heating of the disk in 0957+561, X-ray fluctuations in the corona should cause variations in the disk emission (e.g., Collier et al. 1999; Kazanas & Nayakshin 2001). From the coronal luminosity associated with the unabsorbed variable flux in the bottom panel of Fig. 1 (see above), we can thus simulate the time-dependent response of the disk and the UV–optical flux variability at the observer’s position. The key idea is to check the lamppost model by comparing simulated and observed records. To generate simulated light curves in the  $U$ ,  $g$  and  $r$  bands, we need to know unabsorbed X-ray fluxes at times different to the observation epochs. Hence, we use a linear interpolation or a polynomial fit to produce X-ray fluxes at any epoch within the X-ray monitoring period, avoiding the estimation of fluxes outside this observation period. Apart from the emission wavelength, simulations of X-ray reprocessing also depend on seven physical parameters:  $M$ ,  $\dot{M}$ ,  $H_X$ ,  $A$ ,  $z$ ,  $\theta$  and  $\mu$ , where  $\theta$  is the observer’s latitude and  $\mu$  is the AGN–observer transmission factor (Braga 2010). At a given wavelength, for each physical parameter, we take either its observed value, or a reasonable range or no prior, and then we fit simulated fluxes to the data shown in the top panel of Fig. 1.

First, X-ray fluxes during the observation period are derived from a linear interpolation, which allows us to produce best-fit simulated UV–optical curves (triangles in Fig. 11) after certain initial epochs (vertical dashed lines in Fig. 11). We assume a corona–disk radiative coupling with three fixed parameters:  $z = 1.41$ ,  $A =$

$0.2$  and  $M = 2.5 \times 10^9 M_\odot$ . The other four quantities,  $\dot{M}$ ,  $H_X$ ,  $\theta$  and  $\mu$ , are treated as free parameters to be optimized by a  $\chi^2$  technique, although we use physically motivated priors to accelerate the optimization process:  $1 \leq \dot{M} \leq 10 M_\odot \text{ yr}^{-1}$ ,  $1 \leq H_X \leq 10 R_S$  and  $10^\circ \leq \theta \leq 80^\circ$ . We obtain the best-fit parameter values  $\dot{M} = 3 M_\odot \text{ yr}^{-1}$ ,  $H_X = R_S$  and  $\theta = 10^\circ$  in the three  $Ugr$  bands. The best fit in the  $U$  band is characterized by  $\mu = 18$  and  $\chi^2/\text{dof} = 9$  (dof = 12; top panel of Fig. 11). We also derive  $\mu = 14.5$  and  $\chi^2/\text{dof} = 8$  in the  $g$  band (dof = 21; middle panel of Fig. 11), and  $\mu = 14$  and  $\chi^2/\text{dof} = 4$  in the  $r$  band (dof = 24; bottom panel of Fig. 11).

Second, we study some variants of the analysis in the middle panel of Fig. 11 ( $g$  band). Instead of a linear interpolation, this time we perform a polynomial fit. The best-fit curve (triangles in the top panel of Fig. 12) is characterized by the parameter values:  $\dot{M} = 3 M_\odot \text{ yr}^{-1}$ ,  $H_X = R_S$ ,  $\theta = 10^\circ$  and  $\mu = 14.5$  ( $\chi^2/\text{dof} = 8$ ). We also consider a larger reflectivity  $A = 0.5$  (e.g., Kazanas & Nayakshin 2001), leading to  $\dot{M} = 2 M_\odot \text{ yr}^{-1}$ ,  $H_X = R_S$ ,  $\theta = 10^\circ$  and  $\mu = 22$  ( $\chi^2/\text{dof} = 7$ ; triangles in the middle panel of Fig. 12). The last variant incorporates the possibility of a 0.1-mJy contamination generated by a source other than the disk. We then derive  $\dot{M} = 2 M_\odot \text{ yr}^{-1}$ ,  $H_X = R_S$ ,  $\theta = 10^\circ$  and  $\mu = 16$  ( $\chi^2/\text{dof} = 7.5$ ; triangles in the bottom panel of Fig. 12). There is no agreement between the best-fit and observed UV–optical light curves (see Figs. 11 and 12), which calls into question the lamppost model in 0957+561.

The reduced  $\chi^2$  values of the best fits in Figs. 11–12,  $\chi^2/\text{dof} \gg 1$ , indicate that the corona–disk radiative coupling does not work in 0957+561. Not even paying attention to the  $\chi^2$ , there are obvious systematic differences between the observed and best-fit curves, and two best-fit parameters have anomalous values. For example,  $\mu = \mu_{lens}\mu_{dust} > 10$  is counterintuitive because  $\mu_{lens} \sim 1$  (see above) and dust extinction must produce  $\mu_{dust} < 1$ . However, although the corona is located on the black hole at  $H_X = R_S$ , the model does not incorporate any general relativistic effect. Thus, the presence of a rotating Kerr black hole may lead to disk illuminations much larger than those predicted by the Newtonian framework (Miniutti & Fabian 2004), avoiding the need for unphysical AGN–observer transmission factors.

Additionally, the best-fit values of  $\theta$  coincide with our lower limit of the observer’s latitude range, i.e.,  $10^\circ$ . This means that  $\theta \leq 10^\circ$ , in clear contradiction with other observations of 0957+561. The observed broad emission lines are consistent with relatively large latitudes, so the expected dust torus around the disk does not intercept the line of sight to the broad-line region (e.g., Antonucci 1993). Moreover, the jet morphology also suggests a relatively large latitude (e.g., Roberts et al. 1985). The small best-fit value of the latitude is an artefact related to the observed UV–optical and X-ray trends, and the standard model we use for connecting them. If the X-ray fluctuation leads the UV–optical variations, then a significant smoothing of the X-ray curve is required to try to reproduce the shape of the low-energy curves (see Fig. 1). In the lamppost model, the maximum smoothing occurs for the minimum latitude, so that very small (implausible) latitudes are favoured.

### 3.3. X-ray reflection

The lamppost model involving a standard corona (see subsection 3.2) is generally supported by evidence of X-ray reflection by cold gas in AGNs (George & Fabian 1991). Two reflection features are a fluorescent 6.4 keV Fe  $K\alpha$  line and a hump in the spectrum above 10 keV. However, our X-ray spectra in Fig. 3 do not contain any flux excess in the 10–25 keV band (source rest-frame), and there is no evidence of the Fe  $K\alpha$  line. This could indicate the presence in 0957+561 of a power-law X-ray source at a large height above the disk (Miniutti & Fabian 2004). Since the further the X-ray emission region is placed, the weaker the Fe  $K\alpha$  line and hump will be, this interpretation naturally explains why 0957+561 does not have significant reflection features.

The measured time lags between the X-ray record and the UV-optical curves (see Table 2) are also consistent with a power-law X-ray source in the direction of the rotation axis and located relatively far from the central black hole. Both the inner disk and X-ray emission region are plausibly irradiated by the driving source in the immediate vicinity of the black hole. Using the average X-ray/UV-optical delay of 32 days and assuming the observer at a typical latitude of  $45^\circ$ , the X-ray source would be at a typical height of  $\sim 0.05$  pc  $\sim 200 R_S$ . This should correspond to the base of the relativistic jet (Junor et al. 1999). A schematic representation of X-ray and UV continuum sources of 0957+561 is drawn in Fig. 13. This scheme can account for all our data in the time and spectral domains.

The central driving source is an elusive structure. It may be a hot torus surrounding the black hole (e.g., Rees et al. 1982) and emitting EUV radiation (energies of tens of eV). This does not induce reflection features at keV energies. Moreover, such a source is unobservable because the UV spectra of both images of 0957+561 are totally absorbed below 2200 Å, i.e., at  $E > 13.6$  eV in the source rest-frame (Michalitsianos et al. 1993). A second candidate is the faint thermal component that we detect in the Chandra X-ray spectra (see Fig. 4). This component could also be associated with a hot and geometrically-thick innermost accretion flow. Simulations of the co-evolution of supermassive black holes and their host galaxies show that the most massive black holes ( $M > 5 \times 10^8 M_\odot$ ) are hosted by giant elliptical galaxies and are rapidly rotating (Fanidakis et al. 2011). Thus, a large fraction of the emitted very soft X-rays might be bent towards the disk by the strong gravitational field of a rotating Kerr black hole, enhancing the disk illumination and severely reducing the emission towards the observer (Miniutti & Fabian 2004). However, even if strong gravity effects are responsible of this anisotropic emission, there is a serious difficulty to invoke the very soft X-rays as the central driving source. For example, the  $g$ -band optical curve in Fig. 1 has two remarkable features: (a) a clear decline between days 5200 and 5250, and (b) a 40% growth from day 5250 to day 5350. These features are quite different from those observed in Fig. 4. Assuming a delay of  $\sim 10$  days between central and  $g$ -band variations (see subsection 3.1), the blackbody X-ray curves can not account for the optical variations: Fig. 4 indicates an increase in flux before day 5240, and constrains a possible growth over days 5240–

5340 to be less than 25% ( $1\sigma$  upper limit from linear fits to the absorbed and unabsorbed fluxes).

### 4. CONCLUSIONS

This paper reports on a concurrent X-ray–UV–optical monitoring of the double  $z = 1.41$  RLAGN 0957+561 over six months, using the Chandra X-ray Observatory, the Swift/UVOT and the Liverpool Robotic Telescope. The continuum light curves for the B image of this gravitationally lensed AGN show prominent intrinsic fluctuations, which were predicted in advance by analysing optical records for the leading (A) image one year before (Goicoechea & Shalyapin 2009). Our new UV–optical records of 0957+561B in the  $U$ ,  $g$  and  $r$  bands are then used to unambiguously detect interband delays of several days,  $U$  leading and  $r$  trailing. A simple scenario can explain these band-to-band delays: a flaring source very close to the central supermassive black hole illuminates a standard accretion disk and induces UV variations at radii of  $\sim 10$ – $20 R_S$ . This finding is similar to those usually found for local AGNs at hundreds of  $R_S$  from central driving sources (e.g., Collier et al. 1998).

We also find a highly significant correlation between the brightness record for the X-ray emission with power-law spectrum and the three UV–optical light curves, with peaks corresponding to a time lag of  $\sim 32$  days, UV–optical leading. This correlation signal at about one month is due to the slow (tens of days in the source rest-frame) components of the X-ray and UV–optical light curves. The X-ray curve is thus significantly delayed from the UV–optical, and it is the opposite of what the accretion paradigm for AGNs predicts. In such a paradigm, the central source driving the variability is a standard corona just above the black hole. This corona emits the observed X-rays with a power-law spectrum, so power-law X-ray variations precede UV–optical ones. We conclude that the standard accretion scenario for AGNs does not account for the echo mapping in 0957+561, since the central driving source can not be a standard corona. Detailed simulations of X-ray reprocessing and the lack of X-ray reflection at keV energies also rule out the possibility that the disk variability is driven by a standard corona. Our observations are consistent with power-law X-ray emission from the jet base. The emission region would typically be located at  $\sim 200 R_S$  from the central dark object (see the global scheme in Fig. 13).

While the monitoring of 0957+561 indicates the presence of a non-standard central driving source, similar studies of fluctuations over tens of days in local AGNs led to a wide variety of results. For example, the X-ray–UV–optical variability of Mrk 79 agreed with the accretion paradigm (Breedt et al. 2009). In this Seyfert nucleus, the height of the standard corona could vary from  $10 R_S$  (high-flux state) to  $3 R_S$  (low-flux state) over 2.5 years. On the opposite side, a 1.5-year monitoring campaign of NGC 3516 showed that the optical variations lead the X-rays by  $\sim 100$  days (Maoz et al. 2000). This result goes against the existence of a driving X-ray source in NGC 3516. Interestingly, the seed photons in 0957+561 could plausibly be attributed to EUV radiation produced near the black hole. They would drive most of the rapid variability and a part of the emission of the rest of the X-ray and UV continuum sources. Some

of these seed photons would be thermally reprocessed into far and middle UV radiation in the standard disk, where viscous heating generates additional non-variable emission; others would be boosted to soft and hard X-rays via inverse Compton scattering at the base of the jet, where additional emission and fast (days) variability is possible (see the bottom panel of Fig. 9). Presumably, the rapid rotation of the black hole (Peng et al. 2006; Fanidakis et al. 2011) disrupts the corona and converts it into the relativistic jet. However, the jet would keep a hot base as a "residual corona".

Besides 0957+561, other RLAGNs also show weak or unresolved humps and Fe K $\alpha$  lines (e.g., Grandi et al. 2006). Thus, most or all massive RLAGNs may contain power-law X-ray sources at relatively large heights above their central black holes, as well as central EUV sources driving their multiwavelength flux variations. Further continuum reverberation studies of low and high-redshift accretion-dominated RLAGNs are needed to check the evolution and universality of this non-standard accretion scenario. The combined reverberation results from past, current and future AGN programmes should reveal the physics in the heart of different AGNs over cosmic time. Finally, we note that a successful reverberation analysis requires a multiwavelength monitoring during a period of strong variability. At  $z \geq 1$ , this task is much easier to plan for a gravitationally lensed AGN, since the variability of some of its images can be predicted in advance based on a modest optical follow-up of the lens system.

Hence, our work opens a new window in reverberation mapping with the use of gravitational lensing.

The authors thank several colleagues and the anonymous referee for their valuable comments on preliminary versions of this paper. We also thank the staff of the Chandra X-ray Observatory (CXO), Liverpool Robotic Telescope (LRT) and Swift Multi-wavelength Observatory (SMO) for their kind interaction and support during the preparation of the project and the observation period. The CXO Center is operated by the Smithsonian Astrophysical Observatory for and on behalf of the National Aeronautics Space Administration (NASA) under contract NAS803060. The LRT is operated on the island of La Palma by Liverpool John Moores University in the Spanish Observatorio del Roque de los Muchachos of the Instituto de Astrofísica de Canarias (ORM-IAC) with support from the UK Science and Technology Facilities Council. The SMO is supported at Penn State University by NASA contract NAS5-00136. This article is also based on observations made with the Nordic Optical Telescope, which is operated on the island of La Palma jointly by Denmark, Finland, Iceland, Norway, and Sweden, in the Spanish ORM-IAC. This research has been supported by the Spanish Department of Science and Innovation grants AYA2007-67342-C03-02 and ESP2006-13608-C02-01, and University of Cantabria funds.

## REFERENCES

- Antonucci, R. 1993, *ARA&A*, 31, 473  
 Arévalo, P., Uttley, P., Lira, P., Breedt, E., McHardy, I. M., & Churazov, E. 2009, *MNRAS*, 397, 2004  
 Blandford, R. D., & McKee, C. F. 1982, *ApJ*, 255, 419  
 Braga, V. F. 2010, *The Lamppost Model for X-ray Reprocessing in AGNs: Simulations and Analysis of Observations*, MSc thesis (Universidad de Cantabria)  
 Breedt, E., et al. 2009, *MNRAS*, 394, 427  
 Campbell, R. M., Corey, B. E., Falco, E. E., Shapiro, I. I., Gorenstein, M. V., Elósegui, P., Marcaide, J. M., & Alvi, K. 1994, *ApJ*, 426, 486  
 Chartas, G., Gupta, V., Garmire, G., Jones, C., Falco, E. E., Shapiro, I. I., & Tavecchio, F. 2002, *ApJ*, 565, 96  
 Collier, S. 2001, *MNRAS*, 325, 1527  
 Collier, S., Horne, K., Wanders, I., & Peterson, B. M. 1999, *MNRAS*, 302, L24  
 Collier, S. J., et al. 1998, *ApJ*, 500, 162  
 Collin-Souffrin, S. 1991, *A&A*, 249, 344  
 Dickey, J. M., & Lockman, F. J. 1990, *ARA&A*, 28, 215  
 Edelson, R. A., & Krolik, J. H. 1988, *ApJ*, 333, 646  
 Fanidakis, N., Baugh, C. M., Benson, A. J., Bower, R. G., Cole, S., Done, C., & Frenk, C. S. 2011, *MNRAS*, 410, 53  
 Gaskell, C. M. 2006, *ASP Conference Series*, 360, 111  
 George, I. M., & Fabian, A. C. 1991, *MNRAS*, 249, 352  
 Goicoechea, L. J., & Shalyapin, V. N. 2009, *ATel*, 2228, 1  
 Goicoechea, L. J., Shalyapin, V. N., & Gil-Merino, R. 2011, *Ap&SS*, 335, 237  
 Grandi, P., Malaguti, G., & Fiocchi, M. 2006, *ApJ*, 642, 113  
 Junor, W., Biretta, J. A., & Livio, M. 1999, *Nature*, 401, 891  
 Kazanas, D., & Nayakshin, S. 2001, *ApJ*, 550, 655  
 Krolik, J. H. 1999, *Active Galactic Nuclei: from the Central Black Hole to the Galactic Environment* (Princeton: Princeton University Press)  
 Kundic, T., et al. 1997, *ApJ*, 482, 75  
 Landt, H., Padovani, P., Giommi, P., Perri, M., & Cheung, C. C. 2008, *ApJ*, 676, 87  
 Li, W., Jha, S., Filippenko, A. V., Bloom, J. S., Pooley, D., Foley, R. J., & Perley, D. A. 2006, *PASP*, 118, 37  
 Magdziarz, P., & Zdziarski, A. A. 1995, *MNRAS*, 273, 837  
 Maoz, D., Edelson, R., & Nandra, K. 2000, *AJ*, 119, 119  
 McLure, R. J., & Dunlop, J. S. 2004, *MNRAS*, 352, 1390  
 Michalitsianos, A. G., et al. 1993, *ApJ*, 417, L57  
 Miniutti, G., & Fabian, A. C. 2004, *MNRAS*, 349, 1435  
 Muñoz-Tuñón, C., Vernin, J., & Varela, A. M. 1997, *A&AS*, 125, 183  
 Netzer, H., & Peterson, B. M. 1997, in *Astronomical Time Series*, ed. D. Maoz, A. Sternberg, & E. M. Liebowitz (Dordrecht: Kluwer), 85  
 Ovaldsen, J. E., Teuber, J., Schild, R. E., & Stabell, R. 2003, *A&A*, 402, 891  
 Pelt, J., Schild, R., Refsdal, S., & Stabell, R. 1998, *A&A*, 336, 829  
 Peng, C. Y., Impey, C. D., Rix, H. W., Kochanek, C. S., Keeton, C. R., Falco, E. E., Lehar, J., & McLeod, B. A. 2006, *ApJ*, 649, 616  
 Poole, T. S., et al. 2008, *MNRAS*, 383, 627  
 Rees, M. J., Begelman, M. C., Blandford, R. D., & Phinney, E. S. 1982, *Nature*, 295, 17  
 Roberts, D. H., Greenfield, P. E., Hewitt, J. N., Burke, B. F., & Dupree, A. K. 1985, *ApJ*, 293, 356  
 Roming, P. W. A., et al. 2005, *Sp. Sci. Rev.*, 120, 95  
 Schneider, P., Ehlers, J., & Falco, E. E. 1992, *Gravitational Lensing* (Berlin: Springer-Verlag)  
 Serra-Ricart, M., Oscoz, A., Sanchis, T., Mediavilla, E., Goicoechea, L. J., Licandro, J., Alcalde, D., & Gil-Merino, R. 1999, *ApJ*, 526, 40  
 Shakura, N. I., & Sunyaev, R. A. 1973, *A&A*, 24, 337  
 Shalyapin, V. N., Goicoechea, L. J., Koptelova, E., Ullán, A., & Gil-Merino, R. 2008, *A&A*, 492, 401  
 Spergel, D. N., et al. 2007, *ApJS*, 170, 377  
 Steele, I. A., et al. 2004, *Proceedings of the SPIE*, 5489, 679  
 Taylor, J. R. 1997, *An Introduction to Error Analysis* (Sausalito, USA: University Science Books)  
 Urry, M. 1998, *Adv. Sp. Res.*, 21, 89  
 Urry, M. 2003, *ASP Conference Series*, 290, 3  
 Walsh, D., Carswell, R. F., & Weymann, R. J. 1979, *Nature*, 279, 381  
 Weisskopf, M. C., et al. 2002, *PASP*, 114, 1

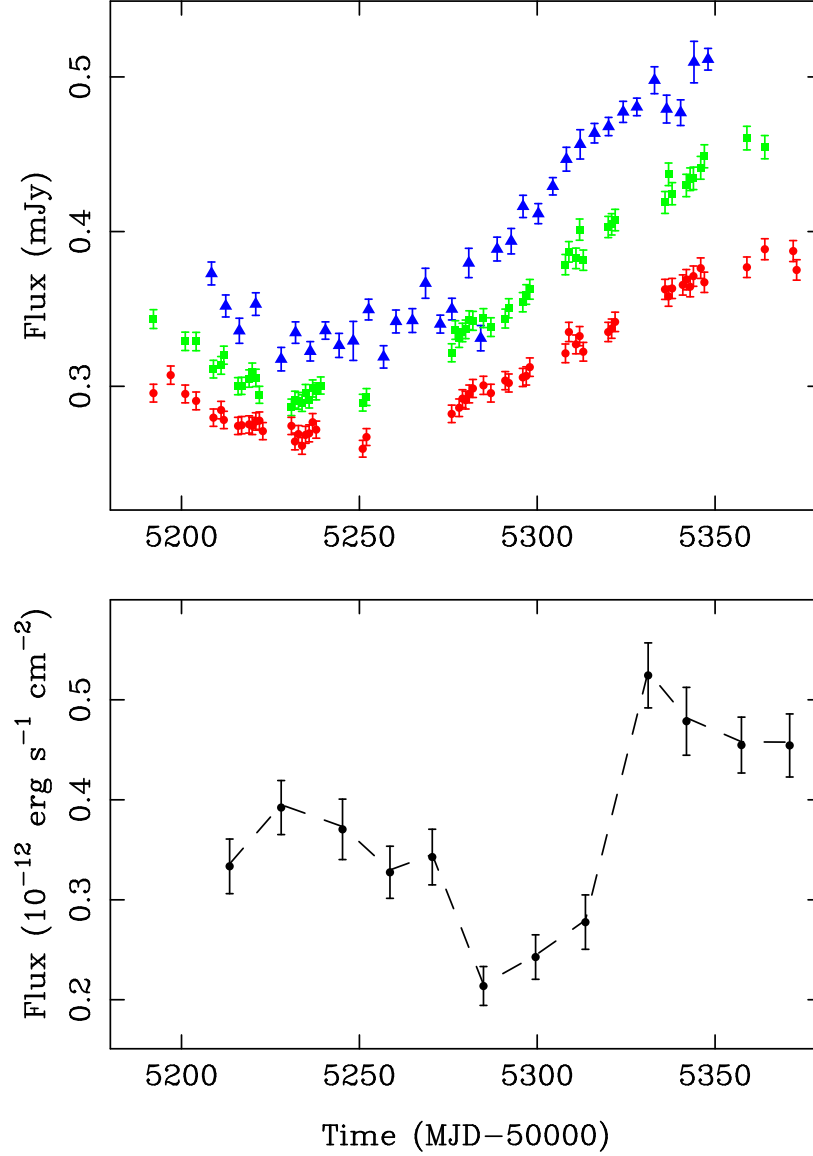


FIG. 1.— Top: Optical and UV light curves of 0957+561B from late 2009 to mid 2010. Triangles (UVOT,  $U$  band), squares (LRT,  $g$  band) and circles (LRT,  $r$  band) are observed fluxes in mJy, associated with sources emitting at  $\lambda = 1438 \text{ \AA}$  (8.6 eV),  $1944 \text{ \AA}$  (6.4 eV) and  $2558 \text{ \AA}$  (4.8 eV), respectively. The optical light curves are vertically shifted by  $-0.13 \text{ mJy}$  ( $g$  band) and  $-0.25 \text{ mJy}$  ( $r$  band) to improve visual comparison. Bottom: Chandra X-ray light curve of 0957+561B from early to mid 2010. Circles are observed fluxes of the power-law X-ray source (range 2–10 keV in the source rest-frame), while the dashed line traces the time evolution of the unabsorbed flux in the same energy range.



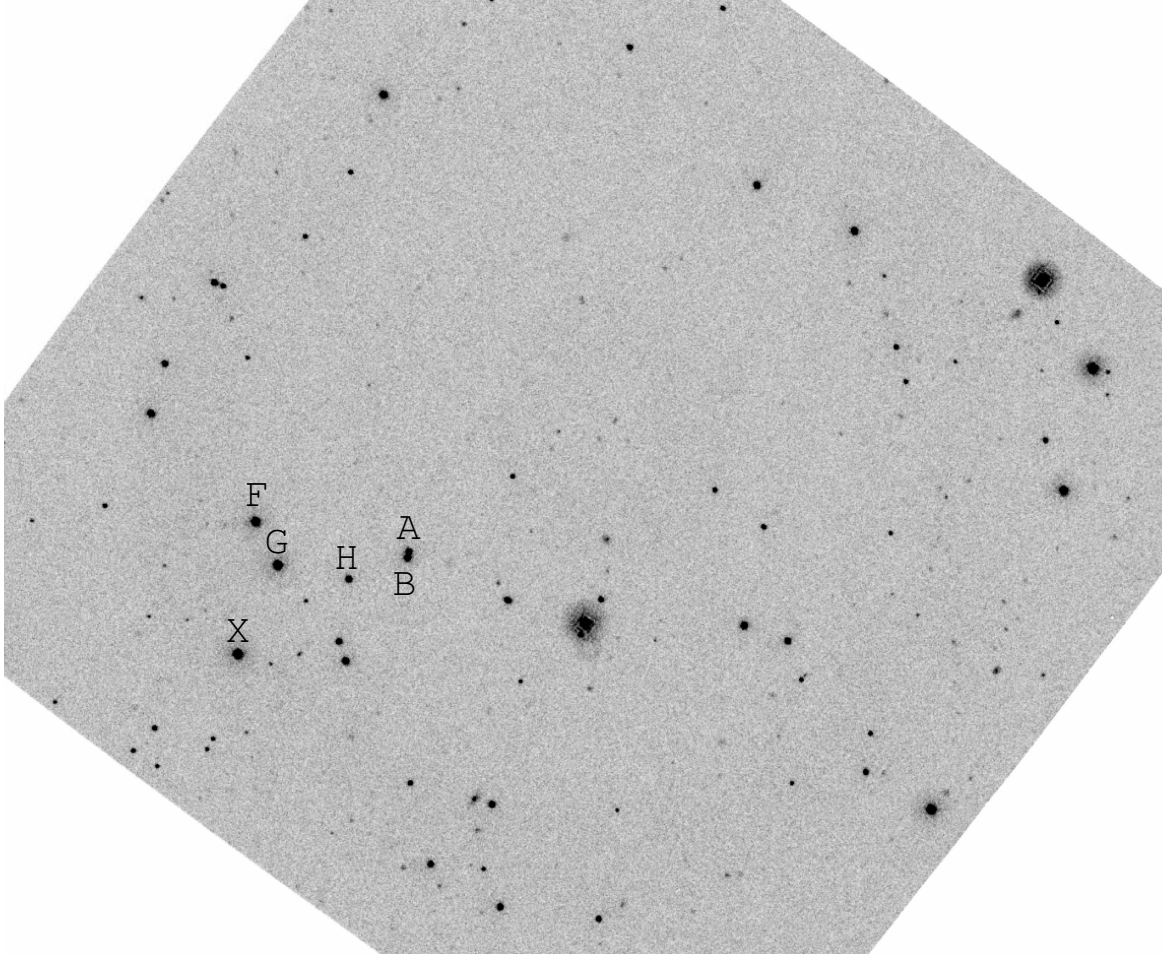


FIG. 2.— Near UV Swift/UVOT frame of the field of 0957+561. This 1092 s exposure was taken on 2010 May 12. The AGN images are labelled A and B, whereas some bright stars close to the AGN are labelled H, X, G and F (e.g., see Fig. 1 of Ovaldsen et al. 2003). There are many additional bright sources within the  $16' \times 16'$  field of view, so the 5-month monitoring campaign can be used to detect new UV variables or to characterize the short-term variability of known variables.

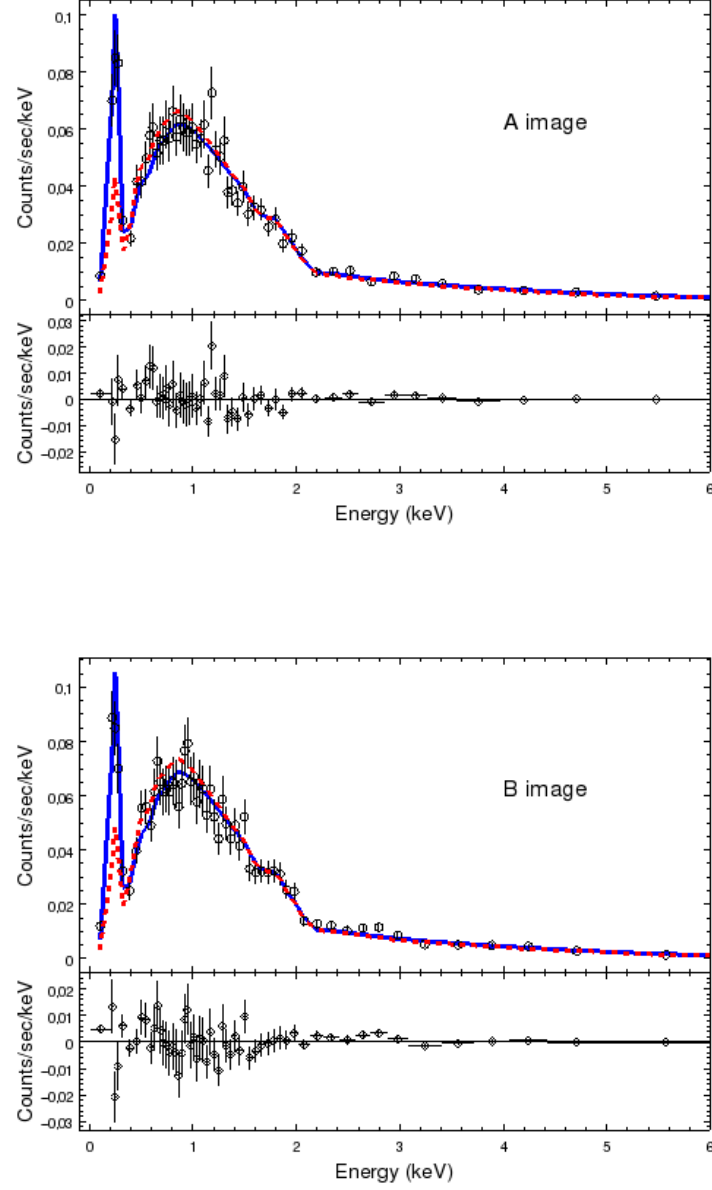


FIG. 3.— Chandra X-ray spectra of 0957+561A and 0957+561B. These spectra are stacked from all observing epochs. An absorbed power-law model produces poor fits to the data ( $\Gamma = 1.9$  and  $\chi^2/\text{dof} = 2.8$ ; dashed lines), whereas a power-law plus blackbody and Galactic absorption model notably improves the fits ( $\Gamma = 1.78$ ,  $kT = 0.08$  keV and  $\chi^2/\text{dof} \sim 1$ ; solid lines). We introduce a blackbody emission to explain the soft excess at energies  $< 0.5$  keV (the horizontal axis represents energy in the observer rest-frame). The residuals for each quasar image (data - solid line) are displayed in the bottom subpanels. We do not find evidence for a Fe  $K\alpha$  line at  $\sim 2.7$  keV (6.4 keV in the source rest-frame) and a hump above 4 keV ( $> 10$  keV in the source rest-frame).

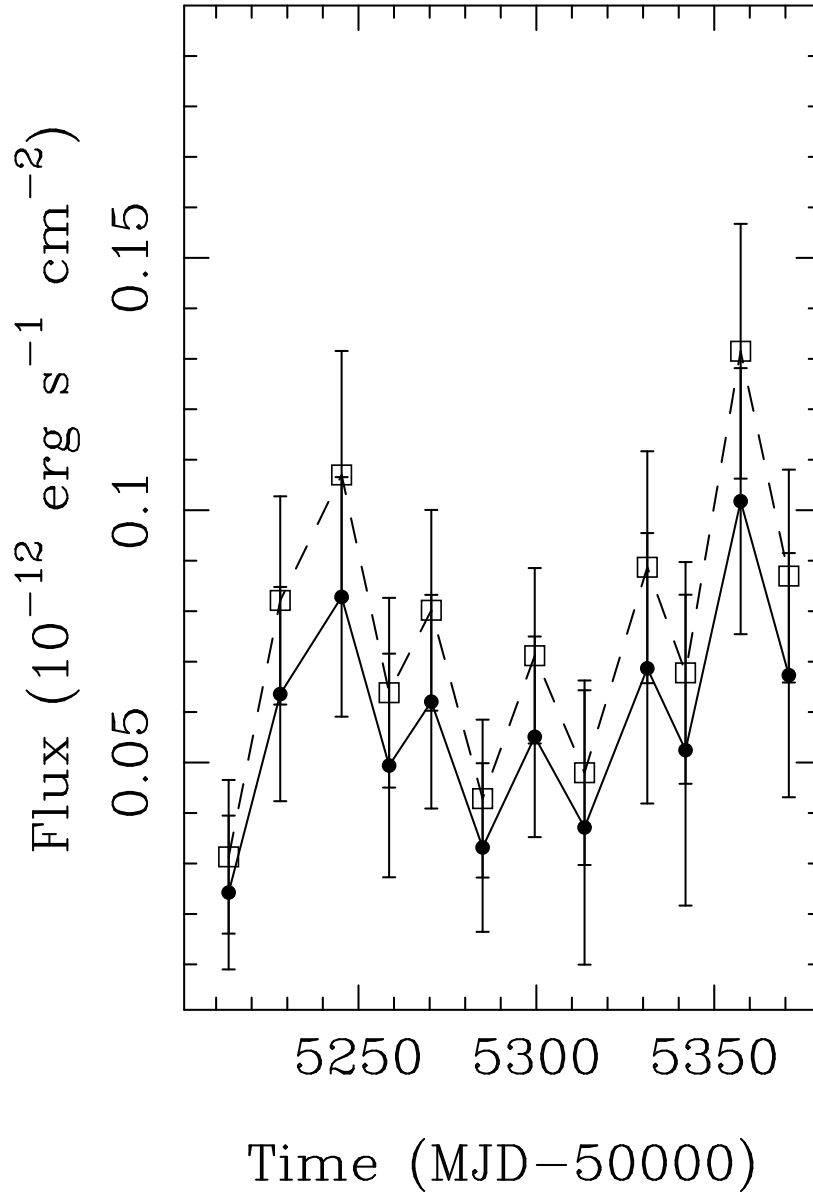


FIG. 4.— Blackbody X-ray light curves of 0957+561B. Circles and squares are observed (absorbed) and unabsorbed fluxes at energies below 1 keV in the source rest-frame. The blackbody component with  $kT = 0.08$  keV is much fainter than the power-law component (see the bottom panel of Fig. 1). The data points have large relative errors that significantly exceed those in the light curves in Fig. 1.

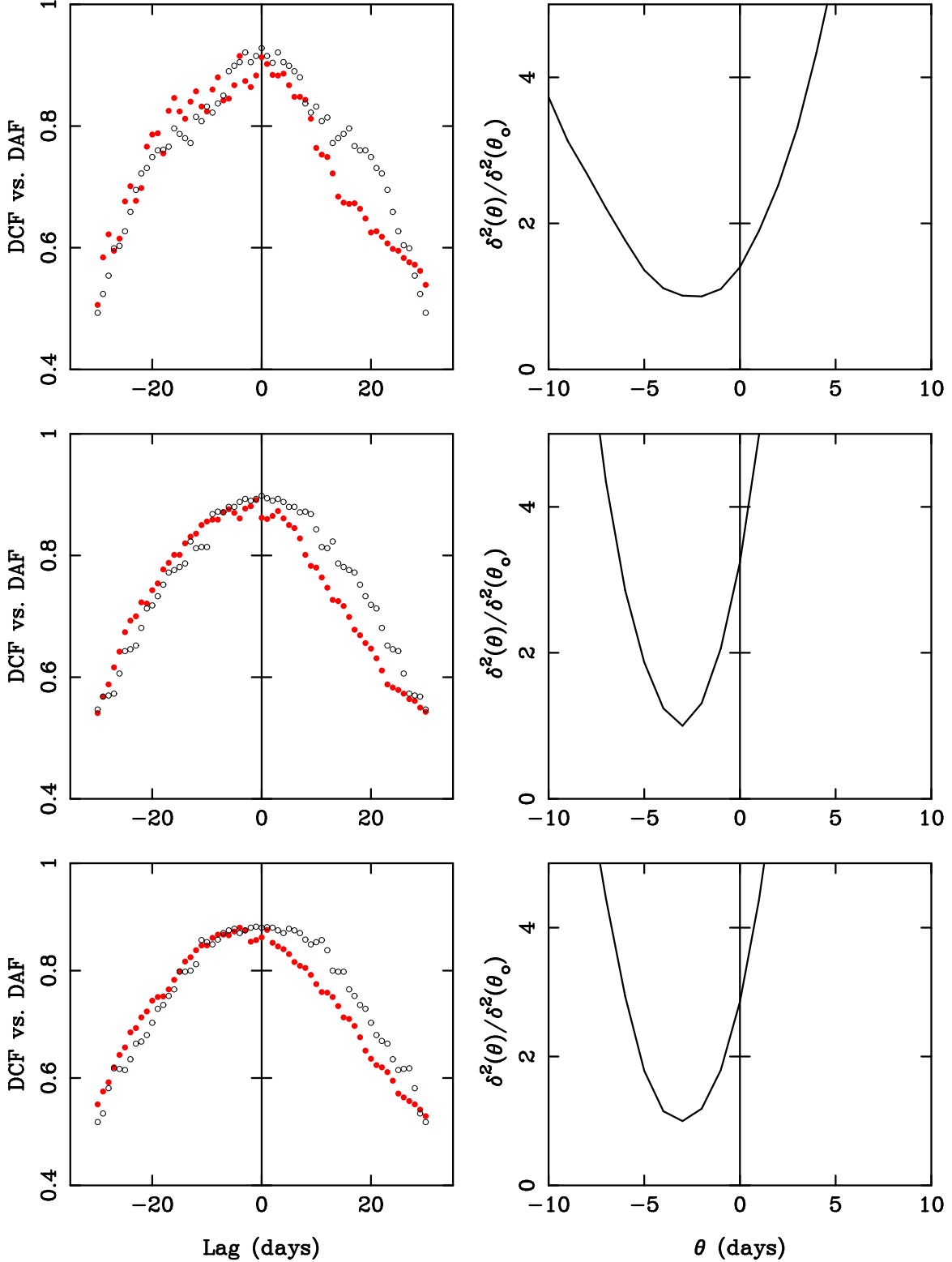


FIG. 5.— Time delay between the  $g$  and  $U$  bands in 0957+561. The left panels show the comparisons between the  $DCF$  (filled circles) and the  $DAF$  (open circles) for three values of the bin semisize  $\alpha$ . While the  $DCF$  is the  $gU$  cross-correlation, the  $DAF$  is the average of the  $gg$  and  $UU$  autocorrelations. In each left panel, there is clear evidence of a  $gU$  time delay, since the  $DAF$  peak should be shifted to the left by several days to optimally match the  $DCF$  delay-peak. Possible values of this time shift  $\theta$  versus the associated  $\delta^2$  values normalised by its minimum value  $\delta^2(\theta_0)$  are displayed in the corresponding right panel (see main text). Top:  $\alpha = 7$  days. Middle:  $\alpha = 10$  days. Bottom:  $\alpha = 12$  days.

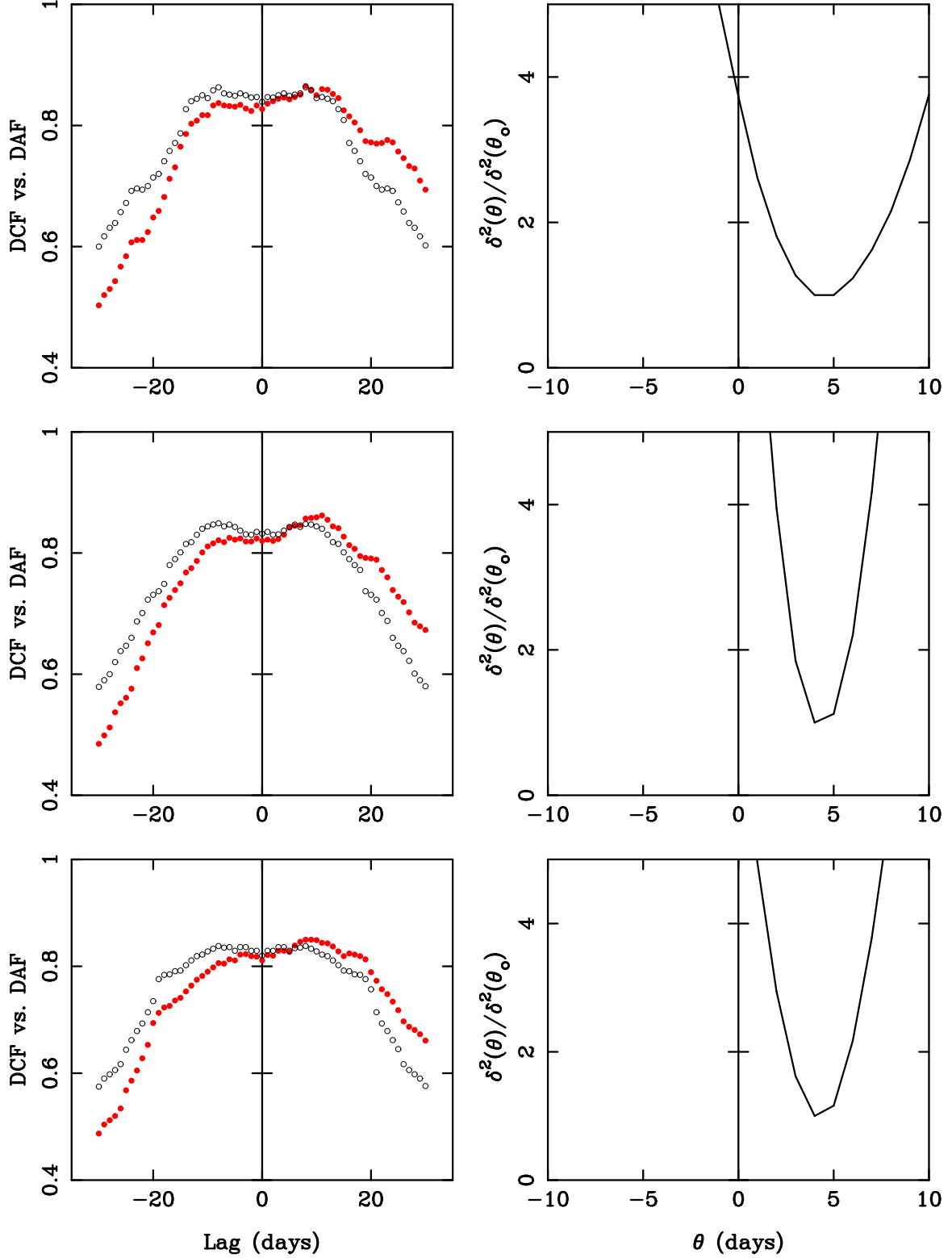


FIG. 6.— Time delay between the  $g$  and  $r$  bands in 0957+561. The  $DCF$  (filled circles) is the  $gr$  cross-correlation, the  $DAF$  (open circles) is the average of the  $gg$  and  $rr$  autocorrelations, and  $\delta^2(\theta)$  is the function to be minimized (see Fig. 5 and main text). In the top, middle and bottom panels, we can observe the presence of a time shift between the  $DCF$  and  $DAF$ , so the  $DAF$  should be shifted to the right by a few days to optimally match the  $DCF$  peak. Top:  $\alpha = 15$  days. Middle:  $\alpha = 18$  days. Bottom:  $\alpha = 20$  days.

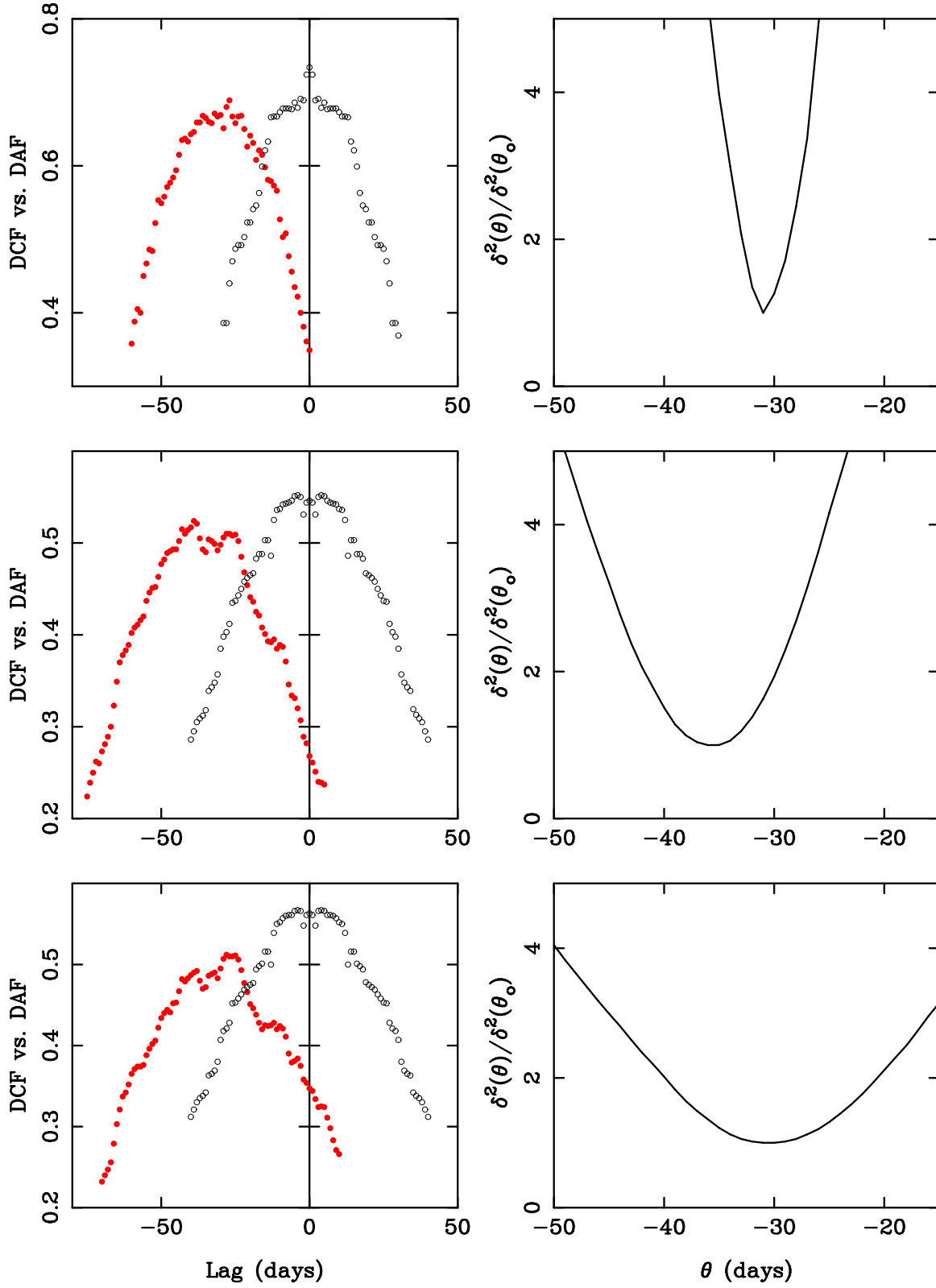


FIG. 7.— Time delay between the power-law X-ray and UV-optical records in 0957+561 (see Figs. 5–6 and main text for basic notation and meaning of symbols). In order to optimally match the *DCF* peak, the *DAF* should be shifted to the left by about one month. Top: *XU* comparison with  $\alpha = 30$  days. Middle: *Xg* comparison with  $\alpha = 45$  days. Bottom: *Xr* comparison with  $\alpha = 45$  days.

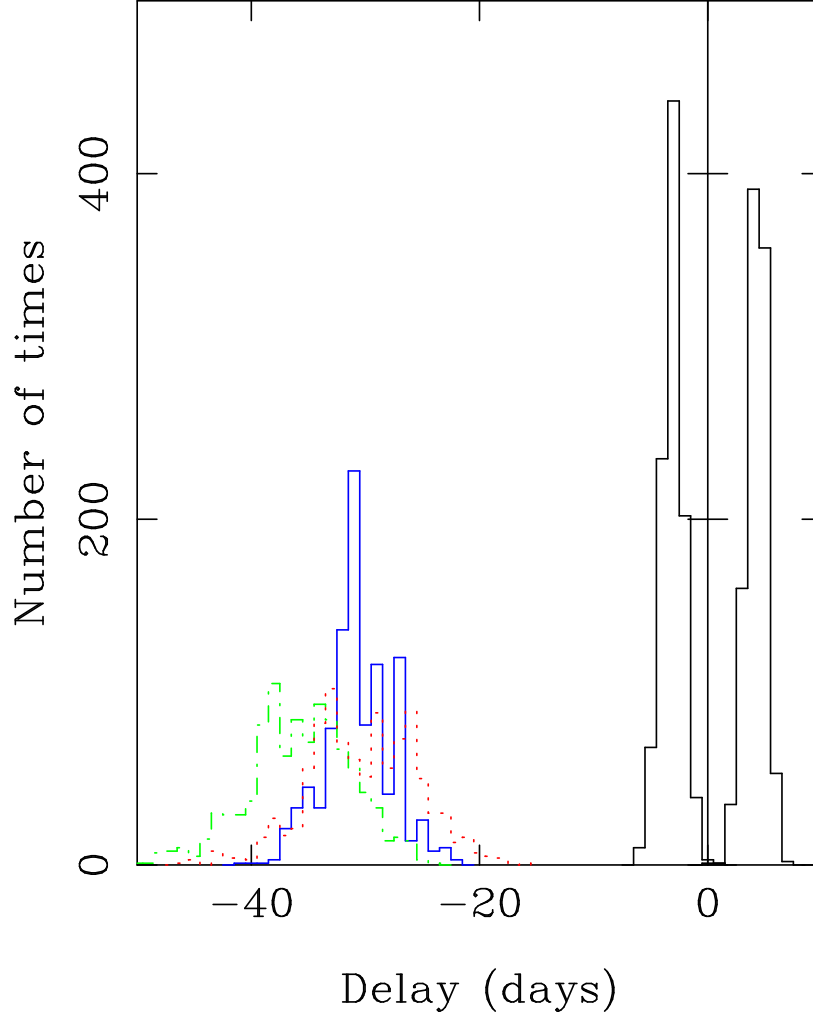


FIG. 8.— Delay distributions. From 1000 simulated repetitions of the original experiment with the LRT, Swift/UVOT and Chandra, we obtain 1000 delay values for each pair of curves  $gU$  (narrow histogram around a delay of  $-3$  days),  $gr$  (narrow histogram around a delay of  $4$  days),  $XU$  (broad histogram drawn with a solid line),  $Xg$  (broad histogram traced by a dashed-dotted line) and  $\bar{X}r$  (broad histogram traced by a dotted line). These distributions allow us to determine time delay errors.

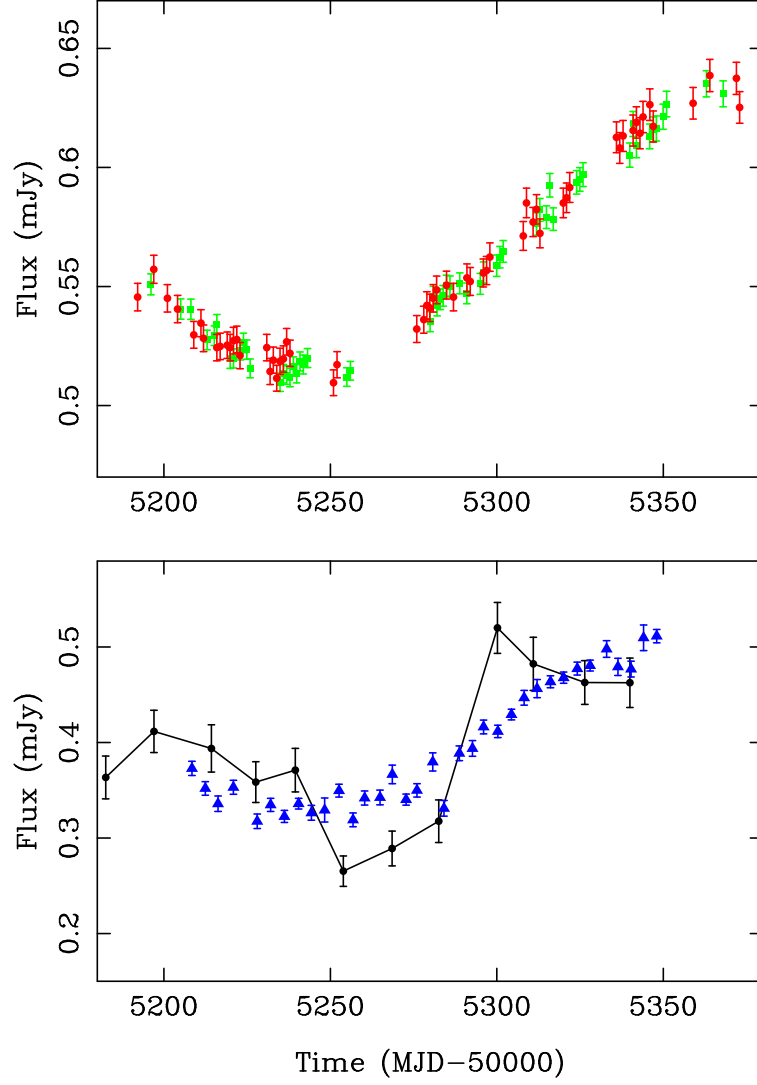


FIG. 9.—  $\chi^2$  comparisons. We use a  $\chi^2$  method to compare two light curves *a* and *b*, obtaining a time delay, a flux offset and a multiplicative factor for the curve *a*. Once these three parameters are known, we put together the shifted and (de)magnified version of the curve *a*, and the curve *b*. Top: *gr* light curves. We infer a delay of 4 days, a flux offset of 0.21 mJy and a demagnification factor of 0.72. The corrected version of *g* and the original version of *r* are represented by squares and circles, respectively. Bottom: *XU* light curves. The  $\chi^2$  technique leads to a delay of -31 days. This time lag, a flux offset of 0.09 mJy and a demagnification factor of 0.82 are used to make the corrected version of *X* (circles and line). The original version of *U* is traced by triangles.



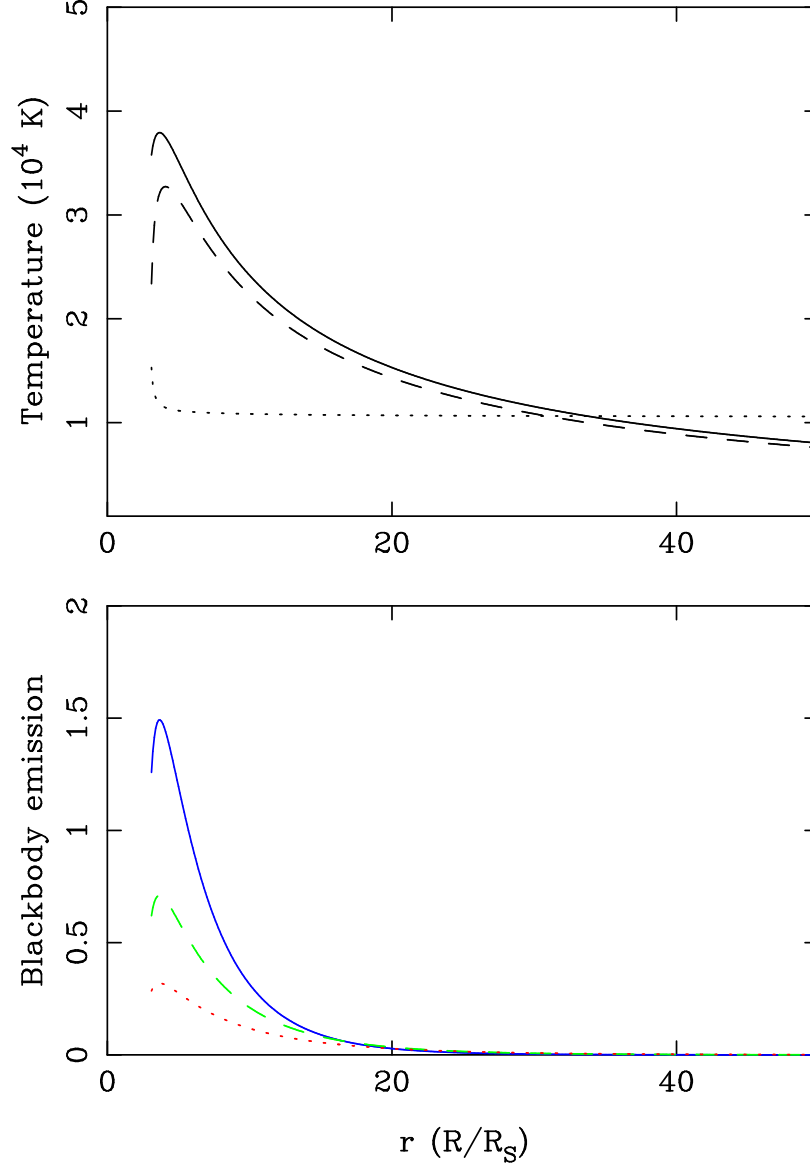


FIG. 10.— Top: Radial temperature profile for an irradiated accretion disk in 0957+561. The dashed and solid lines represent  $T_{vis}$  and the total temperature  $T = (T_{vis}^4 + T_{irr}^4)^{1/4}$ , respectively. The dotted line describes the ratio  $T/T_{vis}$ . As usual, the inner radius of the disk is set to  $3 R_S$ . Bottom: Blackbody emission profile of the disk at different wavelengths. The solid, dashed and dotted lines correspond to blackbody sources at  $\lambda = 1438 \text{ \AA}$ ,  $1944 \text{ \AA}$  and  $2558 \text{ \AA}$ , respectively. The radial emission profile (Planck function in arbitrary units) of the three sources is enhanced in the vicinity of the innermost ring at  $R = 3R_S$ .

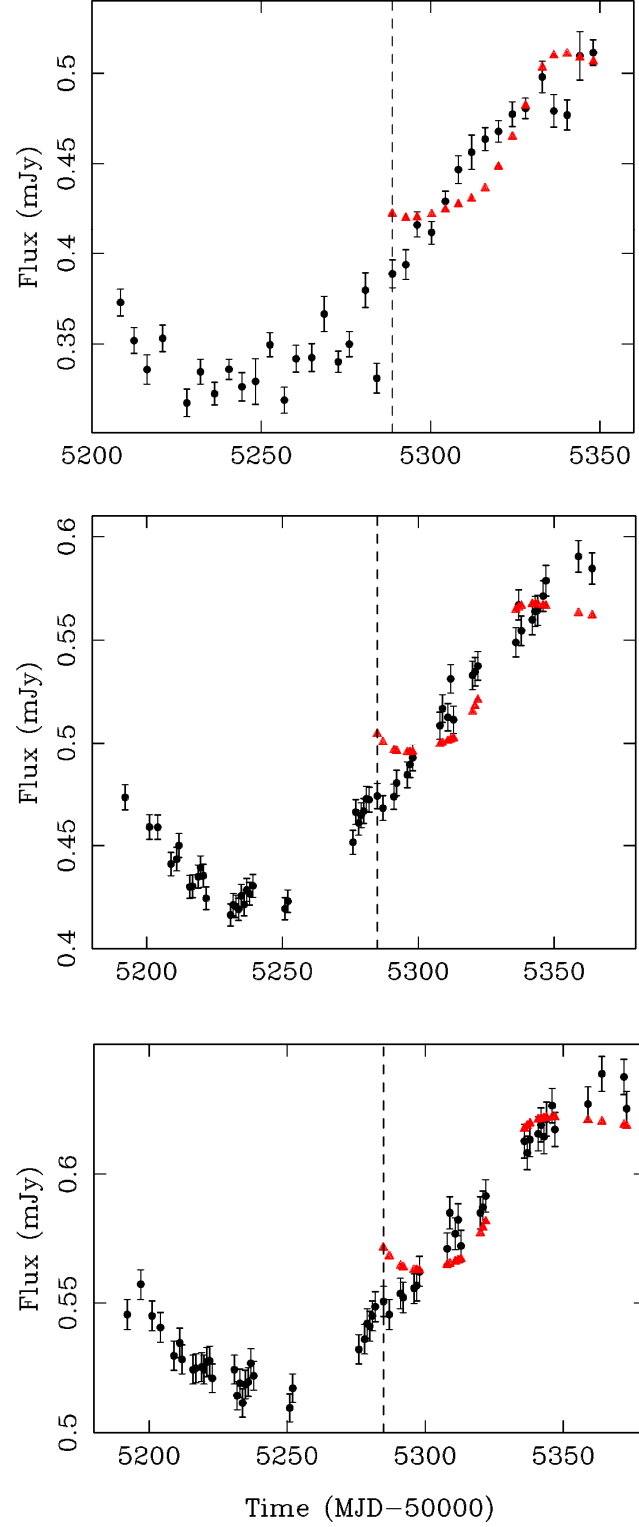


FIG. 11.— X-ray reprocessing in 0957+561. X-ray fluxes at any epoch within the X-ray monitoring period are derived from a linear interpolation procedure. These fluxes are then used to create simulated UV-optical records, and to carry out  $\chi^2$  fits between the simulated and observed curves (see main text). The observed *Ugr* fluxes are represented by circles, and the best-fit simulated *Ugr* curves are traced by the triangles after the vertical dashed lines. Top: *U* band. Middle: *g* band. Bottom: *r* band.

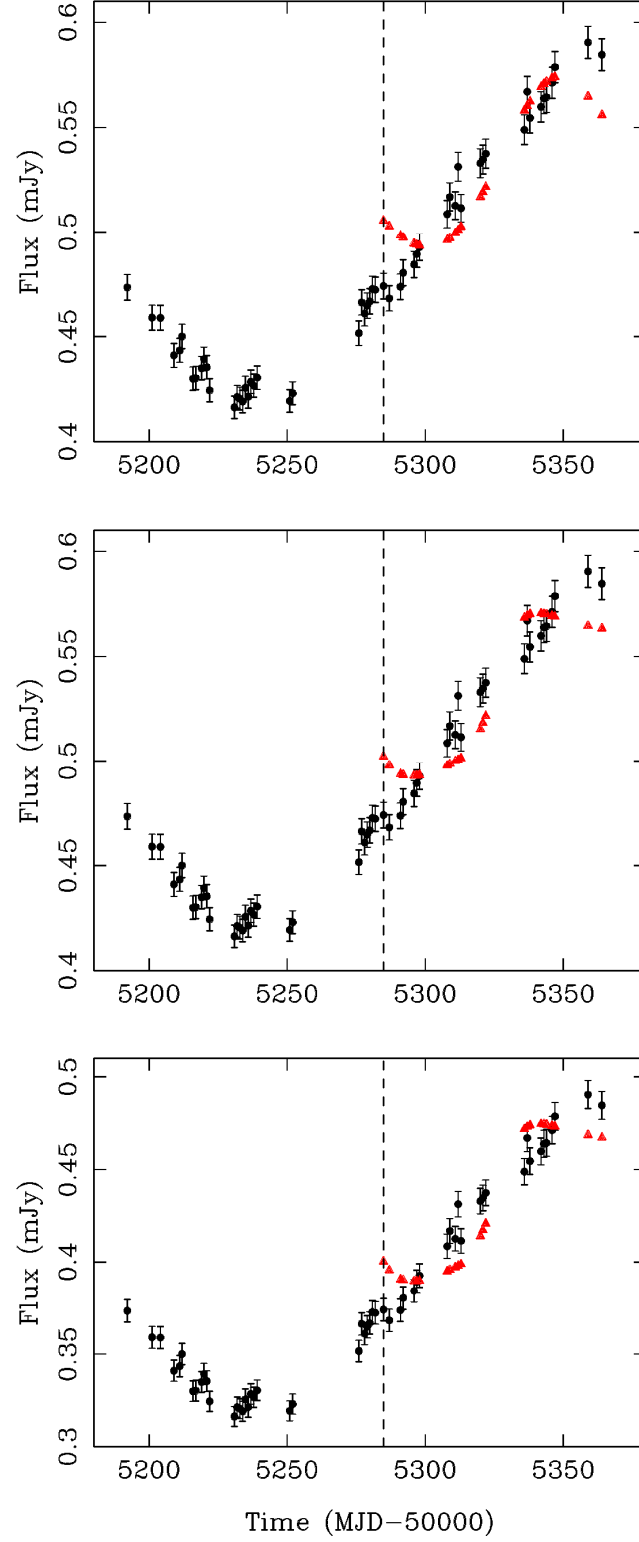


FIG. 12.— Thermal reprocessing of X-rays into  $\lambda = 1944 \text{ \AA}$  ( $g$  band) radiation in 0957+561. We show some variants of the analysis in the middle panel of Fig. 11. The observed  $g$ -band record is traced by circles, while triangles describe the best-fit curves. Top: X-ray fluxes during the observation period are estimated from a 7-degree polynomial resulting from a good fit to the X-ray data. Middle: The disk reflectivity or albedo is increased to  $A = 0.5$ . Bottom: We subtract a possible constant contamination from the observed  $g$ -band curve. The constant extra-disk flux is set to 0.1 mJy.

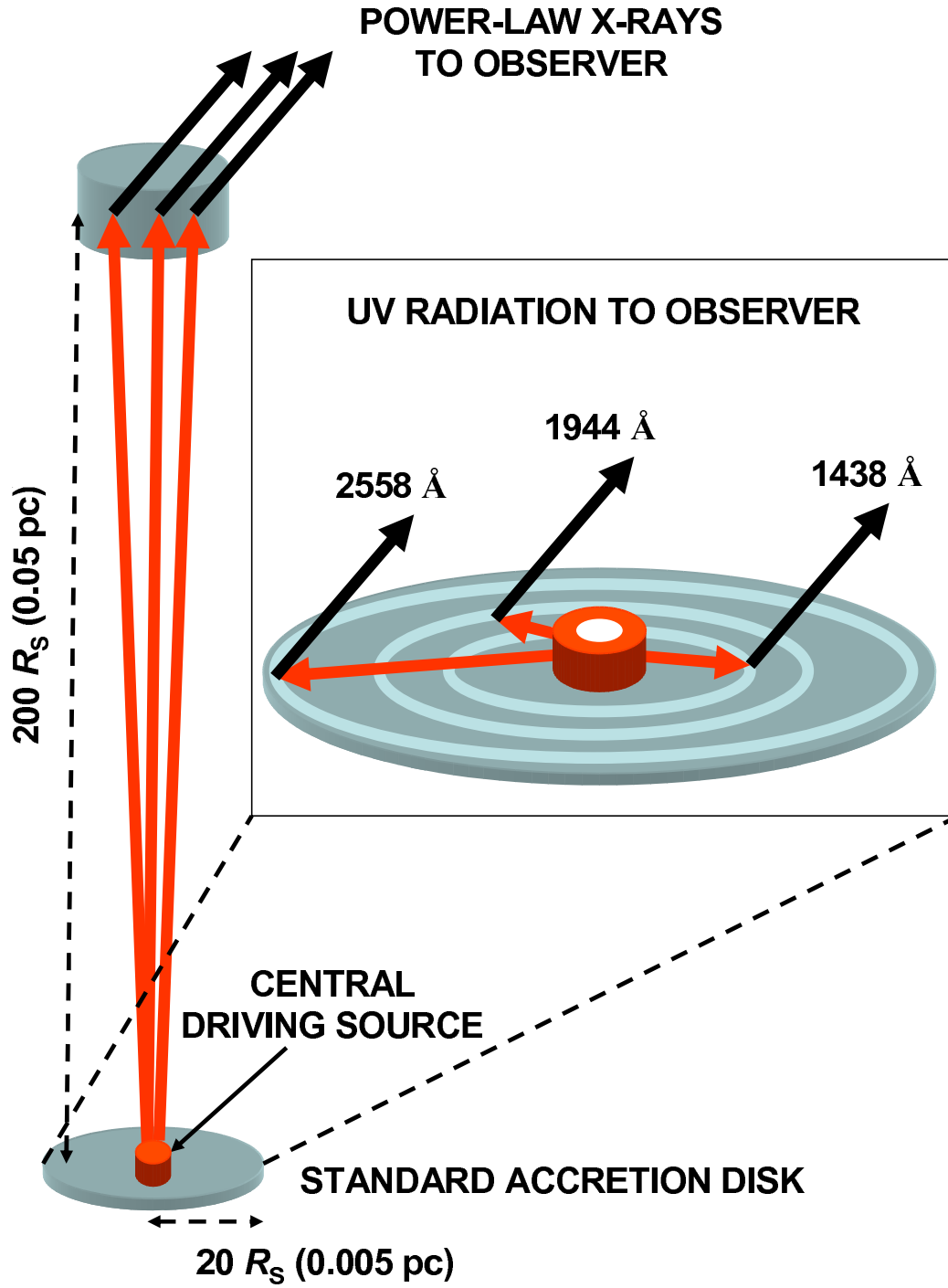


FIG. 13.— Schematic interpretation of the results (see main text).

TABLE 1  
0957+561 MONITORING DATA.

Instrumentation	Obs. mode <sup>a</sup>	Start/end dates	Exposures (ks) <sup>b</sup>
LRT/RATCam/ <i>gr</i> filters <sup>c</sup>	IMAG–M	2009 Dec 26/2010 Jun 25	0.12
Swift/UVOT/CCD/ <i>U</i> filter <sup>d</sup>	IMAG–M	2010 Jan 12/2010 Jun 1	$\sim 0.5$
Chandra/HRMA/ACIS–S3 <sup>e</sup>	SPEC–M	2010 Jan 17/2010 Jun 23	$\sim 3$

<sup>a</sup>The basic observing modes were imaging (IMAG) and spectroscopy (SPEC). The label –M means that the observation scheme was repeated on a regular basis between the start and end dates, i.e., monitoring campaign.

<sup>b</sup>The exposure times in ks refer to each filter or spectrometer on a single night.

<sup>c</sup>Programmes CL09B03 and CL10A02.

<sup>d</sup>Target ID 31567.

<sup>e</sup>Programme 10708333.

TABLE 2  
TIME LAGS (IN DAYS) BETWEEN  
MULTIWAVELENGTH RECORDS OF  
0957+561.

<i>a</i>	<i>b</i>	$\Delta\tau_{ab}$	Comment
<i>g</i>	<i>U</i>	$-3 \pm 1$	<i>U</i> leading
	<i>r</i>	$4 \pm 1$	<i>g</i> leading
<i>X</i>	<i>U</i>	$-31 \pm 3$	<i>U</i> leading
	<i>g</i>	$-35.5 \pm 4.5$	<i>g</i> leading
	<i>r</i>	$-31 \pm 5$	<i>r</i> leading

NOTE. — We compare records in the *Ugr* UV–optical bands and the X–ray region.  $\Delta\tau_{ab} = \tau_b - \tau_a$ , and all measurements are 68% confidence intervals.